EES Batteries

Accepted Manuscript

This article can be cited before page numbers have been issued, to do this please use: J. Noh, S. Yu, S. Lee, W. Kim, K. Yoon, S. Han, J. Song, K. Oh, C. Park, D. Won, G. Choi, K. Lee and K. Kang, *EES Batteries*, 2026, DOI: 10.1039/D6EB00070C.

View Article Online
DOI: 10.1039/D6EB00070C

View Article Online
DOI: 10.1039/D6EB00070C

Broader context statement

All-solid-state batteries require safe, cost-effective solid electrolytes to replace conventional flammable liquid systems. Halide solid electrolytes have emerged as highly promising candidates due to their intrinsic combination of excellent oxidative stability, favorable cathode compatibility, and suitable mechanical deformability. Among them, Li_2ZrCl_6 is particularly attractive owing to the earth-abundant zirconium that provides a substantial economic advantage. However, its practical implementation is bottlenecked by intrinsically low ionic conductivity. While traditional aliovalent doping improves transport, it relies on expensive, scarce elements without a clear understanding of the underlying mechanistic kinetics.

In this work, we reveal that reducing the electrostatic repulsive force from metal cations is the fundamental key to enhancing lithium diffusion in the trigonal Li_2ZrCl_6 framework. This weakened electrostatic environment unlocks previously inaccessible face-sharing pathways and induces local lithium accumulation to facilitate concerted migration. Building on these insights, we introduce a "zero-cost" vacancy-mediated substitution strategy ($Li_{2+4x}Zr_{1-x}Cl_6$) that maximally suppresses electrostatic repulsion. Achieving an enhanced ionic conductivity of 0.8 mS cm^{-1} and superior rate capability, this study establishes a fundamental design principle for developing economically viable, high-performance Zr-based solid electrolyte for next-generation energy storage.

View Article Online
DOI: 10.1039/D6EB00070C

Unlocking Superionic Conduction by Modulating Electrostatic Interactions in a Zirconium-Based Trigonal Halide Solid Electrolyte

*Joohyeon Noh[ad†], Seungju Yu[ad†], Sunyoung Lee[ad], Wonju Kim[ad], Kyungho Yoon[a], Sangwook Han[ad], Junhyuk Song[a], Kyungbae Oh[a], Chanwoong Park[ad], Daero Won[ad], Geunji Choi[ad], Kangtaek Lee[ad] and Kisuk Kang[*abcd]*

[a] Department of Materials Science and Engineering, Research Institute of Advanced Materials (RIAM), Seoul National University, 1 Gwanak-ro, Gwanak-gu, Seoul 08826, Republic of Korea

[b] Center for Nanoparticle Research, Institute for Basic Science (IBS), Seoul National University, 1 Gwanak-ro, Gwanak-gu, Seoul 08826, Republic of Korea

[c] Institute of Engineering Research, College of Engineering, Seoul National University, 1 Gwanak-ro, Gwanak-gu, Seoul 08826, Republic of Korea

[d] Institute for Rechargeable Battery Innovation, Seoul National University, 1 Gwanak-ro, Gwanak-gu, Seoul 08826, Republic of Korea

† These authors contributed equally to this paper

Corresponding authors

Correspondence to Kisuk Kang, matlgen1@snu.ac.kr

Keywords: All-solid-state batteries, Halide solid electrolyte, Aliovalent substitution

View Article Online
DOI: 10.1039/D6EB00070C

Abstract

Halide solid electrolytes have recently emerged as promising candidates for solid-state batteries, combining high ionic conductivity, favorable cathode compatibility, and mechanical softness. Among them, the zirconium-based halide Li_2ZrCl_6 has attracted attention due to its cost advantages over rare-metal-based counterparts, but its intrinsic ionic conductivity remains insufficient for practical applications. While aliovalent substitution has been explored to improve the performance, the mechanisms governing lithium transport and dopant interactions remain unclear. In this study, we systematically investigate how aliovalent cation substitution modulates lithium diffusion within the trigonal Li_2ZrCl_6 framework. By integrating computational and experimental approaches, we show that reducing electrostatic repulsion between cations and lithium ions not only facilitates local lithium diffusion near substituted sites but also unexpectedly generates additional diffusion pathways beyond conventional doping effects, resulting in a more robust percolated diffusion network. Building on these insights, we propose a simpler, dopant-free strategy based on vacancy-mediated substitution, yielding $Li_{2.3}Zr_{0.925}Cl_6$ that exhibits rapid hopping kinetics and enables efficient lithium incorporation, resulting in significantly enhanced ionic conductivity along with improved rate capability and stability. This work reveals a clear composition-path dependency on structurally tolerant halide solid electrolytes, offering a viable route toward high-performance, cost-efficient solid electrolytes.

Introduction

All-solid-state batteries have gained considerable attention as a safer alternative to conventional lithium-ion batteries which pose significant safety risks due to their flammable organic liquid electrolytes[1-4]. However, the practical implementation of all-solid-state batteries

View Article Online
DOI: 10.1039/D6EB00070C

has been consistently plagued by persistent interfacial challenges between solid electrolytes and conventional electrodes[5-8]. In this context, halide-based solid electrolytes, particularly chloride variants, have emerged as promising candidates for catholyte due to their intrinsic combination of excellent oxidative stability and suitable mechanical deformability[9, 10], overcoming the respective limitations of inherently brittle oxide- and chemically reactive sulfide-based electrolytes[11-15]. Among halide superionic conductors with various structures[16-19], the trigonal framework has emerged as a versatile and promising structural platform capable of accommodating a diverse range of metal cations including Yb, Tb, Dy, Ho, Y, and Er[16, 20-24]. Thus, it has not only inspired continuous exploration of new variants but has also provided an expansive compositional landscape to systematically tune and optimize their properties[25, 26]. However, the practical deployment of this family remains constrained, as the accessible compositional space has been predominantly limited by scarce and costly rare-metal cations.

In this respect, Li_2ZrCl_6 has garnered considerable attention as the earth-abundant zirconium element provides a significant economic advantage, which can be even more favorable than that of state-of-the-art sulfide electrolytes considering the elemental cost[27]. Furthermore, Li_2ZrCl_6 features a unique combination of desirable properties for catholyte, including high oxidative stability, mechanical compatibility with electrode materials, and tolerance to ambient humidity[28, 29]. However, its common polymorphic trigonal Li_2ZrCl_6 exhibits intrinsically low ionic conductivity (~4×10^{-4} S cm^{-1} at 30°C), markedly inferior to those of other superionic conductors by more than an order of magnitude, presenting a critical bottleneck to practical implementation. To overcome this limitation, aliovalent substitution has been widely explored as the prevailing strategy to enhance the ionic conductivity of Li_2ZrCl_6. In particular, incorporating trivalent cations[29-33] such as Y^{3+}, Er^{3+}, Dy^{3+}, In^{3+}, or Fe^{3+} was proven to be capable of forming stable solid-solution with significantly improved ionic conductivities reaching ~10^{-3} S cm^{-1}. However, most of these substitution approaches were possible only

View Article Online
DOI: 10.1039/D6EB00070C

with the scarce elements which could form a similar trigonal framework, facing the fundamental limitations regarding economic viability[30-33]. Substituting with an earth-abundant element like Fe^{3+} often led to poor cycling performance due to the undesirable redox activity of Fe[29]. Moreover, despite extensive experimental efforts in cation substitution strategies, it remains elusive how a small amount of dopants could enhance the overall lithium diffusion kinetics in the structure, obscuring the choice of rational dopant strategies.

Herein, we investigate governing factors of lithium-ion transport in the trigonal Li_2ZrCl_6 and reveal general cation interactions that critically shape the energy landscape of diffusion paths in the structure[24, 34]. By systematically examining the pristine Li_2ZrCl_6 with a low-valent-dopant substituted system, such as divalent Zn^{2+}, we elucidate how the presence of dopants impacts overall and site-specific lithium-ion mobility. It is shown that the effective interaction between dopant and lithium yields two-fold effects in reshaping the lithium percolation landscape. The partial substitution of Zr^{4+} with a low-valent dopant unlocks face-sharing pathways that were previously inaccessible due to the strong electrostatic repulsion from Zr^{4+}. Moreover, this additional accessibility culminates in local lithium accumulation, which in turn triggers correlated migration behavior. Consequently, the additional accessible pathways and cooperative motion establish a robust and interconnected percolation network for superior ionic transport. Building on this insight, we synthesize low-valent-dopant substituted systems, and verify that a significant enhancement in the ionic conductivity is possible not only for the Zn-doped case ($Li_{2+2x}Zn_xZr_{1-x}Cl_6$ ($0<x\leq0.25$)) but also for vacancy-mediated substitution with even greater extent in the improvement ($Li_{2+4x}Zr_{1-x}Cl_6$, ($0<x\leq0.25$)). Finally, we demonstrate the superior electrochemical performance of all-solid-state batteries employing vacancy-doped $Li_{2.3}Zr_{0.925}Cl_6$ paired with $LiNi_{0.83}Co_{0.11}Mn_{0.06}O_2$ cathodes. At 0.5C, the cell delivers a high specific capacity of 155 mAh g^{-1}, significantly surpassing that of the pristine Li_2ZrCl_6 cell (120

View Article Online
DOI: 10.1039/D6EB00070C

mAh g^{-1}). Furthermore, the enhanced capacity was complemented by long-term stability, maintaining 75% retention after 300 cycles at 0.5C.

Results and Discussion

Aliovalent substitution in trigonal halide superionic conductor

Li_2ZrCl_6 exhibits a layered-type structure characterized by a hexagonal close-packed (*hcp*) anion framework within the $P\bar{3}m1$ space group, as depicted in Figure 1a. Zr ions occupy either 1a or 2d Wyckoff position octahedral sites, exhibiting a partially disordered arrangement in neighboring *ab*-planes. Lithium ions occupy octahedral sites that share their edges with Zr ions along the *ab*-plane, resulting in a distinctive inverse honeycomb arrangement ($ZrLi_6$) similar to $LiMn_6$ in Li_2MnO_3[35], as shown in the lower panel of Figure 1a. In this *hcp* anion framework, lithium migration within the *ab*-plane should proceed *via* intermediate tetrahedral sites that share a face with the Zr^{4+} octahedron, while interlayer migration along the *c*-axis should occur through direct hopping to neighboring octahedral sites that edge-share with the Zr^{4+} octahedron. It indicates that all primary diffusion pathways are intimately linked to the occupancy and distribution of Zr^{4+} octahedra and their strong electrostatic repulsion[24, 36, 37]. In comparison to the structurally analogous halide solid electrolytes such as Li_3YCl_6 and Li_3InCl_6 with trivalent ions, the migration barrier for lithium ions for both intra- and interplane diffusion would be more significantly affected by the presence of the tetravalent Zr^{4+} ion. In this context, we performed a detailed lithium diffusion analysis on the intrinsic Li_2ZrCl_6 structure along with those doped with low-valent cations comparatively. We selected Zn^{2+} as a model low-valent cation due to its similar ionic radius (0.74 Å) to Zr^{4+} (0.72 Å) for the structural integrity[38]. Furthermore, we examined the hypothetical system with the lowest-valent cation, *i.e.*, zero-

View Article Online
DOI: 10.1039/D6EB00070C

valent vacancy, by locally removing the Zr^{4+} cation (See Supplementary Note 1 for discussion about thermodynamic stability of vacancy-substituted structures).

The lithium diffusion behaviors of these three systems were first probed by conducting *ab initio* molecular dynamics (AIMD) simulations (See computational details in Experimental method and Figures S2a–c and S3 for details). Figure 1b illustrates the overall ionic conductivities estimated at 300 K along with the *ab*-plane (blue) and *c*-axis (red) components for respective cases. It reveals that the ionic conduction of the pristine Li_2ZrCl_6 is highly anisotropic, with the fast *c*-axis conduction and negligible *ab*-plane diffusion. This indicates that despite the layered *hcp* framework, the sluggish *ab*-plane diffusion acts as the primary bottleneck, rendering the macroscopic conduction effectively one-dimensional[24]. On the other hand, the results show that low-valent cation doping leads to a significant enhancement of the *ab*-plane lithium conduction kinetics, yielding a more than two-fold increase in the overall ionic conductivity. The ionic conductivity within the *ab*-plane increases by over four-fold, while that of the *c*-axis does by only a factor of ~1.5, suggesting that the dominant increase in the *ab*-plane conduction resulted in the enhancement in the total ionic conductivity. It also indicates that the low-valent cation doping is specifically beneficial in expediting *ab*-plane diffusion, hinting at a unique path-dependent role of the dopant cation in the trigonal Li_2ZrCl_6 structure.

To visualize the local change in diffusion behaviors upon cation substitution, we analyzed the lithium probability density for pristine Li_2ZrCl_6, Zn-doped $Li_{2.17}Zn_{0.08}Zr_{0.92}Cl_6$, and vacancy-doped $Li_{2.33}Zr_{0.92}Cl_6$, as depicted in Figures 1c–e, respectively. The yellow regions depict the connectivity of lithium probability density, *i.e.*, diffusion pathway, while dashed boxes in each figure highlight the most distinct change observed in the pathways upon dopant substitution. Whereas the pathways near unsubstituted Zr^{4+} sites remain largely unchanged for both doped

View Article Online
DOI: 10.1039/D6EB00070C

cases, those in the vicinity of the substituted sites broaden progressively, which appear to be greater with the zero-valent vacancy dopant. To elucidate this phenomenon, we meticulously analyzed the hopping rates for each *ab*-plane and *c*-axis from the AIMD simulations, which are provided in Figure S4[39]. The results indicated that the hopping rates of both the substituted and neighboring layers increased significantly, consistent with the conductivity enhancement trend. On the other hand, non-substituted layers showed minimal changes in hopping rates in any direction. For the substituted layer, the *ab*-plane hopping rates increased from 8.8×10^9 s^{-1} in Li_2ZrCl_6 to 1.70×10^{10} s^{-1} in $Li_{2.17}Zn_{0.08}Zr_{0.92}Cl_6$ and further to 2.18×10^{10} s^{-1} in $Li_{2.33}Zr_{0.92}Cl_6$, corresponding to an overall increase of approximately 2.5 times. Similarly, the hopping rate in the neighboring layer increased to more than twice its initial value across the same series. In contrast, the *c*-axis hopping rates displayed a relatively modest rise, from 3.20×10^{10} s^{-1} in Li_2ZrCl_6 to 4.66×10^{10} s^{-1} in $Li_{2.33}Zr_{0.92}Cl_6$. These results suggest that the enhancement is related to specific local geometry associated with low-valent dopants in the migration pathway, requiring a more detailed, path-by-path analysis to fully elucidate the governing mechanism.

Localized change in lithium diffusion kinetics induced by aliovalent substitution

We carefully examined local diffusion pathways, which proceed particularly through sites sharing an edge or face with the dopant site (brown octahedron) as illustrated in Figure 2a. The lithium diffusion pathways with this specific local environment could be identified as **Path A** and **Paths B/C**, along *c*-axis and *ab*-plane directions, respectively. In **Path A**, a lithium ion migrates through an intermediate octahedral site that shares an edge with the dopant site. **Path B** represents the in-plane migration on the intralayer involving tetrahedral intermediate sites face-sharing with the dopant site, while **Path C** is that involving the octahedral intermediate

View Article Online
DOI: 10.1039/D6EB00070C

sites face-sharing with the dopant in the neighboring layer. We found that the broadened diffusion pathway in the vicinity of the dopant sites in Figures 1d and 1e is attributed to enhanced accessibility through **Paths B** and **C**. As shown in Figures 2b and S5, the substitutions activate entirely new channels that are inaccessible in pristine Li_2ZrCl_6 especially for **Paths B** and **C**. While the strong repulsion from the Zr^{4+} ion renders the face-sharing intermediate sites in **Paths B** and **C** inaccessible in pristine Li_2ZrCl_6[24], the lower-valence substituents such as Zn^{2+} and vacancy could mitigate the electrostatic repulsion, which in turn lower the activation barriers. Notably, the opening of new diffusion pathways could aid in forming percolated diffusion network within the *ab*-plane by connecting the isolated diffusion clusters, indicated by a red hexagonal ring in Figure S5a[24].

Hopping rates estimated from AIMD simulations quantitatively supported the observed broadening and opening of the diffusion pathways for all relevant diffusion paths (**Paths A**, **B**, and **C**), as presented in the left panel of Figure 2c[39]. A systematic increase in hopping rate was observed as the valence of the substituted metal cations decreased from Zr^{4+} to Zn^{2+} and further to vacancies, most notably for **Path B**. Vacancy substitution led to an increase of nearly two orders of magnitude in the hopping rate compared to pristine Li_2ZrCl_6 in **Path B** (from 0.147 to 5.42 and 13.8×10^{10} s^{-1} for Li_2ZrCl_6, $Li_{2.2}Zn_{0.1}Zr_{0.9}Cl_6$, and $Li_{2.33}Zr_{0.92}Cl_6$, respectively). The enhanced kinetics could be further confirmed by nudged elastic band (NEB) calculations to determine the activation barrier associated with each diffusion path, in the right panel of Figure 2c and Figure S6. For interlayer transport along the *c*-axis (**Path A**), a moderate, stepwise reduction in the barrier is observed, from 254 meV for pristine Li_2ZrCl_6 to 197 meV for Zn^{2+} substitution and 171 meV for vacancy substitution. A far more dramatic effect is observed for the *ab*-plane face-sharing pathways (**Paths B** and **C**). These routes, initially prohibited in the pristine Li_2ZrCl_6 with high activation barrier (> 500 meV), become accessible upon

View Article Online
DOI: 10.1039/D6EB00070C

substitution. Compared to the pristine framework, vacancy substitution yields the most dramatic drop in activation barriers for **Paths B** and **C** (to approximately 145 and 264 meV, respectively), surpassing even the reductions achieved by Zn^{2+} substitution (212 and 273 meV, respectively). The fact that the magnitude of kinetic enhancement exhibits a strong dependence on the valence state of dopant provides compelling evidence that the local electrostatic environment is the dominant governing factor. Given the shorter distance and stronger electrostatic repulsion between the metal cation and lithium ion at face-sharing sites, the *ab*-plane pathways exhibit heightened sensitivity to the electrostatic environment governed by the cation valence (See Supplementary Note 2 for discussion about steric effect on diffusion kinetics).

Another important consequence of low-valent substitution is the occurrence of the extra lithium content to compensate for the charge balance and its spatial redistribution in the structure. According to the analysis of the lithium occupancy of each *ab*-plane in Figure S4 and the lithium probability density in Figures 1c–e, we could detect that the extra lithium ions predominantly redistribute into the substituted plane and its adjacent layers, with a strong tendency to aggregate near the low-valent dopant sites. Given that the collective motion of lithium ions inherently dictates the macroscopic diffusion within the Li_2ZrCl_6 framework[40, 41], we elucidate that this localized aggregation of extra lithium ions effectively establishes lithium-rich channels conducive to rapid lithium conduction[42] near substituted planes, amplifying the probability of concerted migration and thereby lowering the overall activation barriers[43, 44]. Crucially, van Hove correlation analysis for our materials, a mathematical tool used to describe how the positions of ions are correlated in both space and time, validates this physical picture, confirming that the collective transport mechanism remains dominant and becomes strengthened in our doped system (Figure S8). Taken together, low-valent substitution not only reduces the activation barrier for lithium diffusion by modulating metal cation-lithium

View Article Online
DOI: 10.1039/D6EB00070C

interactions but also provides highly favorable conditions for concerted migration by establishing lithium-rich channels, thereby improving lithium hopping kinetics.

Synthesis and evaluation of the doped-Li_2ZrCl_6

Inspired by our theoretical guidance, we synthesized the Zn^{2+} and vacancy-substituted series, $Li_{2+2x}Zn_xZr_{1-x}Cl_6$ and $Li_{2+4x}Zr_{1-x}Cl_6$ ($0<x\leq0.25$), *via* a mechano-chemical route using stoichiometric mixtures of metal chlorides. Figures 3a and 3b present the X-ray diffraction data for the structural analysis of $Li_{2+2x}Zn_xZr_{1-x}Cl_6$ and $Li_{2+4x}Zr_{1-x}Cl_6$, respectively, which indicate that both series retain the characteristic trigonal symmetry of Li_2ZrCl_6. The pristine framework remains largely intact at low dopant concentrations up to x = 0.1, confirming the successful incorporation of the dopants into the host lattice without significant structural distortion. Rietveld refinement results for X-ray diffraction (Figures S9 and S10) further substantiate the structural integrity of the trigonal host across the substitution series. However, the slight transition becomes apparent at a higher substitution level of x = 0.25, with additional reflections alongside the parent peaks, which correspond to those typically seen in disordered cubic close-packed (*ccp*) halide structures (*e.g.*, LiCl, Li_3InCl_6[45], and Li_3ScCl_6[46]). This tendency of partial transition aligns with established principles that the *ccp* structure is preferred over *hcp* framework with higher ionic potentials of lithium and metal in layered lithium halides[47] (See Supplementary Note 3 for details). We further scrutinized the detailed structures of representative samples, Li_2ZrCl_6, $Li_{2.2}Zn_{0.1}Zr_{0.9}Cl_6$, and $Li_{2.3}Zr_{0.925}Cl_6$, by performing high-resolution neutron diffraction, as presented in Figures 3c–e. The Rietveld refinements confirmed the trigonal *hcp* lattice as a dominant phase with the successful incorporation of the dopants into the host particularly within the doping range of $x \leq 0.1$ (See Tables S1–3 for details). Additionally, we conducted X-ray absorption spectroscopy (XAS) analysis on the

View Article Online
DOI: 10.1039/D6EB00070C

doped samples, which did not reveal any significant structural deviations except for the slight atomic rearrangement expected for dopant substitution (Figures S11, S12, and Table S4).

The ionic transport properties of these samples were comparatively analyzed and summarized with respect to measured ionic conductivity and activation barrier in Figures 3f, 3g, and S13. The vacancy-substituted series exhibits a marked enhancement, reaching a peak conductivity of 8×10^{-4} S cm^{-1} at 30°C for $Li_{2.3}Zr_{0.925}Cl_6$ (x = 0.075), which is more than twice that of pristine Li_2ZrCl_6 (3.6×10^{-4} S cm^{-1} at 30°C). The Zn^{2+}-substituted series also shows an increase in conductivity with maximum value of 6.4×10^{-4} S cm^{-1} for $Li_{2.2}Zn_{0.1}Zr_{0.9}Cl_6$ (x = 0.1) at 30°C. A clear performance hierarchy emerges as the effective charge of the cation sublattice is systematically reduced, whereby the ionic conductivity exhibits a commensurate increase as the valency decreases from Zr^{4+} to Zn^{2+}, and ultimately to zero-valent vacancies. We further note that the relative densities of the cold-pressed pellets are comparable across all three compositions (75.8%, 77.8%, and 76.8%, for Li_2ZrCl_6, $Li_{2.2}Zn_{0.1}Zr_{0.9}Cl_6$, and $Li_{2.3}Zr_{0.925}Cl_6$, respectively), confirming that the observed enhancements are intrinsic to the doping effect rather than densification degree (Figure S14). Both $Li_{2.3}Zr_{0.925}Cl_6$ and $Li_{2.2}Zn_{0.1}Zr_{0.9}Cl_6$ displayed lower activation energies (0.351 eV and 0.355 eV, respectively) in comparison to Li_2ZrCl_6 (0.370 eV), strongly suggesting that a weakened electrostatic environment reshapes the energy landscape for lithium-ion migration. Notably, the ionic conductivity of both series follows a volcano-shaped dependence on the substitution level, where the conductivity decline beyond the optimal doping level is attributed to the partial phase transition to the disordered *ccp* phase with intrinsically lower mobility[48-51] (See Supplementary Notes 3 for details). Nevertheless, the realization of significant conductivity enhancement with only small amount of substitution, even with such structural constraints, strongly validates the efficacy of our theoretical design.

View Article Online
DOI: 10.1039/D6EB00070C

Beyond the improved ionic transport, it is crucial to verify whether these doping strategies compromise the intrinsic electrochemical stability of the host framework. To further assess this, cyclic voltammetry was performed on the pristine Li_2ZrCl_6 alongside the optimal compositions of each doping strategy, $Li_{2.2}Zn_{0.1}Zr_{0.9}Cl_6$ and $Li_{2.3}Zr_{0.925}Cl_6$ (Figures S15 and S16). The electrochemical stability window is largely preserved upon doping, with no significant shift in either the oxidative or reductive onset potentials (~4.0 V and ~1.8 V *vs.* Li/Li^+, respectively). In particular, the oxidative current is predominantly confined to the first cycle and diminishes markedly in subsequent sweeps, indicative of stable passivation layer formation at high voltages.

Electrochemical performance of the doped-Li_2ZrCl_6 in solid-state batteries

The electrochemical properties of the solid electrolytes were tested for samples with the highest ionic conductivities, *i.e.*, $Li_{2.2}Zn_{0.1}Zr_{0.9}Cl_6$ and $Li_{2.3}Zr_{0.925}Cl_6$, in a solid-state battery setup using a commercial-level single crystal high-nickel cathode ($LiNi_{0.83}Co_{0.11}Mn_{0.06}O_2$) as the active material. Figure 4a presents the first cycle profile of these cells at 0.1C (where 1C = 200 mA g^{-1}) within a voltage range of 3.0–4.3 V (*vs.* Li/Li^+). At 0.1C, the solid-state cells employing doped electrolytes exhibited electrochemical profiles comparable to the pristine Li_2ZrCl_6. They delivered comparably high initial discharge capacities of 194.5 and 196 mAh g^{-1} with initial coulombic efficiencies of 86.6% and 88%, respectively, mirroring the robust performance of the pristine counterpart (197 mAh g^{-1}, 86%). This confirms that the electrochemical reversibility inherent to the halide framework is well-preserved even after doping. On the other hand, the rate capability of the cells shows a strong correlation with the ionic conductivity of solid electrolyte, with performance disparities becoming more pronounced at higher current densities, as shown in Figure 4b. Notably, at a practical rate of

View Article Online
DOI: 10.1039/D6EB00070C

0.5C, the cell utilizing $Li_{2.3}Zr_{0.925}Cl_6$ outperformed its counterparts, delivering a discharge capacity of 155 mAh g^{-1} which corresponds to a retention of 78.9% relative to the specific capacity at 0.1C. This stands in clear distinction to the $Li_{2.2}Zn_{0.1}Zr_{0.9}Cl_6$ and pristine Li_2ZrCl_6 cells, which yielded lower capacities of 137 mAh g^{-1} and 120 mAh g^{-1} with corresponding retentions of 70.7% and 60.8%, respectively. The mechanistic origin of this kinetic hierarchy was further elucidated by galvanostatic intermittent titration technique and electrochemical impedance spectroscopy analyses (Figures S17 and S18). The progressive substitution from Zr^{4+} to Zn^{2+} and to zero-valent vacancies systematically reduces both the bulk electrolyte resistance and the interfacial charge transfer resistance, indicating that the enhanced ionic conductivity facilitates Li^+ transport at both the bulk and interfacial levels within the composite cathode. Beyond its superior rate capability, the cell incorporating $Li_{2.3}Zr_{0.925}Cl_6$ demonstrated robust long-term durability. It successfully delivered a higher discharge capacity at 0.5C without compromising the cyclability inherent to the pristine framework, as shown in Figure 4c. After 300 cycles, the cell retained approximately 75% of its initial capacity, a value comparable to those of the pristine counterparts. This confirms that significant kinetic enhancement was achieved without sacrificing electrochemical stability. The versatility of the optimized electrolyte was further corroborated in $LiCoO_2$ cells, as illustrated in Figures S19 and S20. Specifically, as highlighted in Figure S20, the cell utilizing $Li_{2.3}Zr_{0.925}Cl_6$ could also retain the high-nickel cathode performance, demonstrating outstanding rate capability and durability. At 1C, it delivered a high specific capacity of 118 mAh g^{-1} with 84% retention relative to 0.1C, outperforming the $Li_{2.2}Zn_{0.1}Zr_{0.9}Cl_6$ (113 mAh g^{-1}, 81%) and pristine Li_2ZrCl_6 (106 mAh g^{-1}, 75%). Furthermore, superior long-term stability was achieved, maintaining 75% of its capacity after 500 cycles compared to 71% for the pristine cell under identical conditions.

To verify the chemical stability of the halide solid electrolyte and its compatibility with the oxide cathode, time-of-flight secondary ion mass spectrometry (ToF-SIMS) was employed to

View Article Online
DOI: 10.1039/D6EB00070C

probe the elemental distribution within cycled composite electrodes consisting of $LiNi_{0.83}Co_{0.11}Mn_{0.06}O_2$ and pristine Li_2ZrCl_6, Zn-, or vacancy-substituted Li_2ZrCl_6. As illustrated in Figure 4d, the distribution of characteristic secondary ion fragments corresponding to the oxide cathode lattice (*i.e.*, Ni-O, Co-O, and Mn-O) remained largely consistent after cycling across all evaluated compositions, indicating that the chemical integrity of the active material is preserved without significant degradation at interface. Simultaneously, we monitored for the emergence of Cl-O and Zr-O signals, which are typical diagnostic indicators of interfacial side reactions or electrolyte decomposition[52]. The insignificant accumulation of these species confirms the superior electrochemical stability of our system, suggesting that no substantial parasitic reactions occur during operation. Furthermore, this chemical robustness was consistently observed in $LiCoO_2$-based cells. As shown in Figures S21 and S22, both XPS and ToF-SIMS analyses revealed minor signal deviations even after extensive cycling, confirming the absence of substantial interfacial degradation and the electrochemical stability of our system.

Summary

This work provides a comprehensive, atomistic-level understanding of the mechanism by which aliovalent substitution enhances lithium-ion transport in the trigonal Li_2ZrCl_6 framework, establishing a principle for the rational design of cost-effective halide electrolytes. Our theoretical investigation revealed that reducing the electrostatic repulsive force exerted by the metal cation is a critical factor in enhancing lithium diffusion kinetics of aliovalent substitution in Li_2ZrCl_6 structure. Substituting Zr^{4+} with a less repulsive ion not only promotes lithium diffusion near substituted site with lithium aggregation, facilitating concerted diffusion behavior, but also opens up new diffusion pathways, which have been prohibited due to strong

View Article Online
DOI: 10.1039/D6EB00070C

electrostatic repulsion from Zr^{4+} in pristine Li_2ZrCl_6. As a proof-of-concept for our theoretical findings, we synthesized both Zn^{2+}- and vacancy-substituted series ($Li_{2+2x}Zn_xZr_{1-x}Cl_6$ and $Li_{2+4x}Zr_{1-x}Cl_6$, where x = 0–0.25). The vacancy-doped $Li_{2.3}Zr_{0.925}Cl_6$ exhibited the highest ionic conductivity of 0.8 mS cm^{-1}, surpassing that of the pristine Li_2ZrCl_6 and best-performing Zn^{2+}-substituted compound, thereby corroborating computational predictions regarding the performance hierarchy. Furthermore, the optimized composition, $Li_{2.3}Zr_{0.925}Cl_6$, demonstrated superior rate capability and robust electrochemical stability, with *ex situ* analysis confirming negligible interfacial degradation. By introducing 'zero-cost' metal vacancies as dopants into the cost-effective Li_2ZrCl_6 framework, our strategy offers an economically viable route to high-voltage halide superionic conductors, bypassing the reliance on expensive rare-earth metals (*e.g.*, Y, In, or Sc).

View Article Online
DOI: 10.1039/D6EB00070C

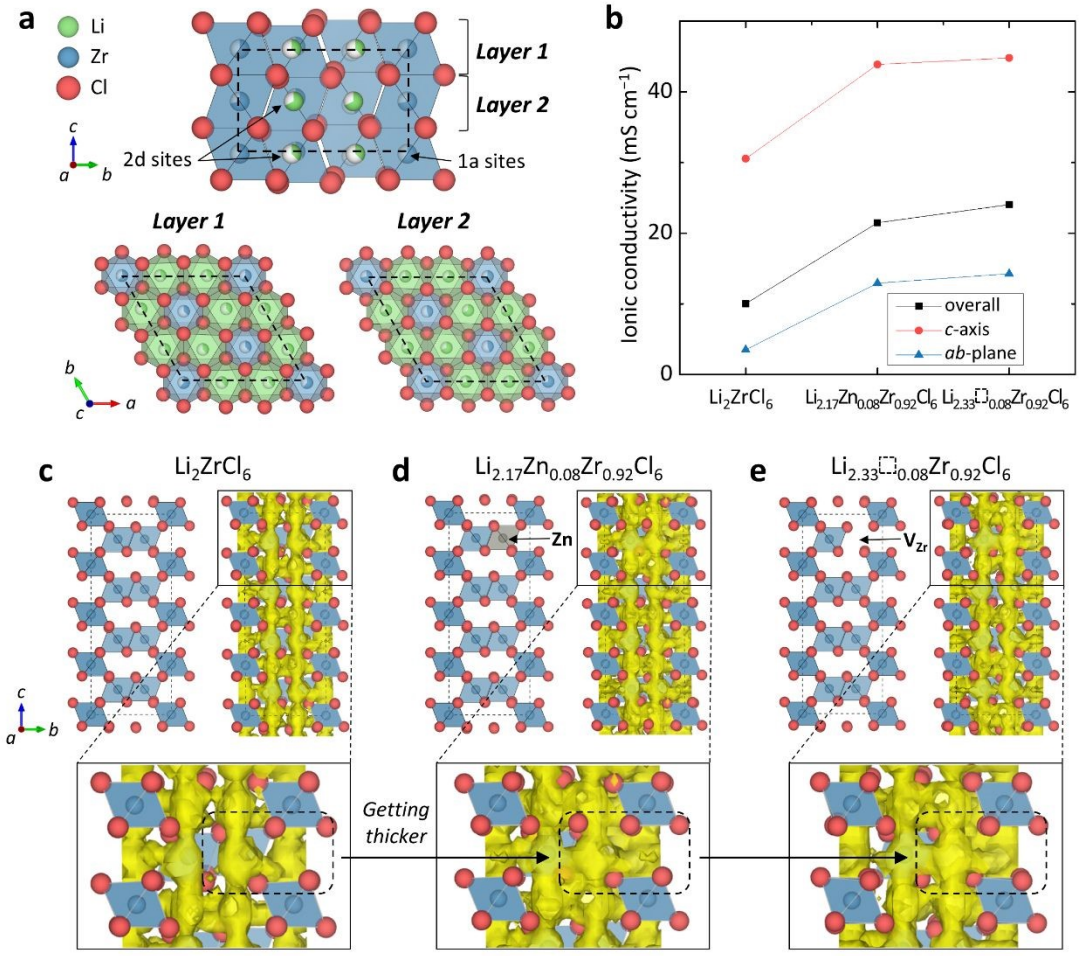

Figure 1. Effect of aliovalent substitution on lithium diffusion properties of trigonal Li_2ZrCl_6. (a) Structural representation of Li_2ZrCl_6 with Zr ion exhibiting partial occupancy at the Wyckoff 1a and 2d sites. The upper panel delineates the overall connectivity and arrangements of Zr 1a and Zr 2d sites. The lower panel depicts the configurations of individual planes, namely Layer 1 and 2**. (b)** Extrapolated ionic conductivity at 300 K for each component (overall, *c*-axis, and *ab*-plane) of Li_2ZrCl_6, $Li_{2.17}Zn_{0.08}Zr_{0.92}Cl_6$, and $Li_{2.33}Zr_{0.92}Cl_6$, obtained from AIMD simulations conducted between 500 K to 700 K. The overall conductivity is represented in black, the *ab*-plane in blue, and the *c*-axis in red. **(c-e)** Iso-surface (yellow) of lithium probability density $\boldsymbol{P = P_{max}/1024}$ at 500 K of three model structures: **(c)** pristine Li_2ZrCl_6, **(d)** Zn^{2+}-substituted $Li_{2.17}Zn_{0.08}Zr_{0.92}Cl_6$, and **(e)** vacancy-substituted $Li_{2.33}Zr_{0.92}Cl_6$, where the vacancy site is denoted as V_{Zr}. The lower panels illustrate enlarged views of the diffusion pathways near the substituent site, with dashed boxes highlighting the expanded diffusion network induced by the substitution.

View Article Online
DOI: 10.1039/D6EB00070C

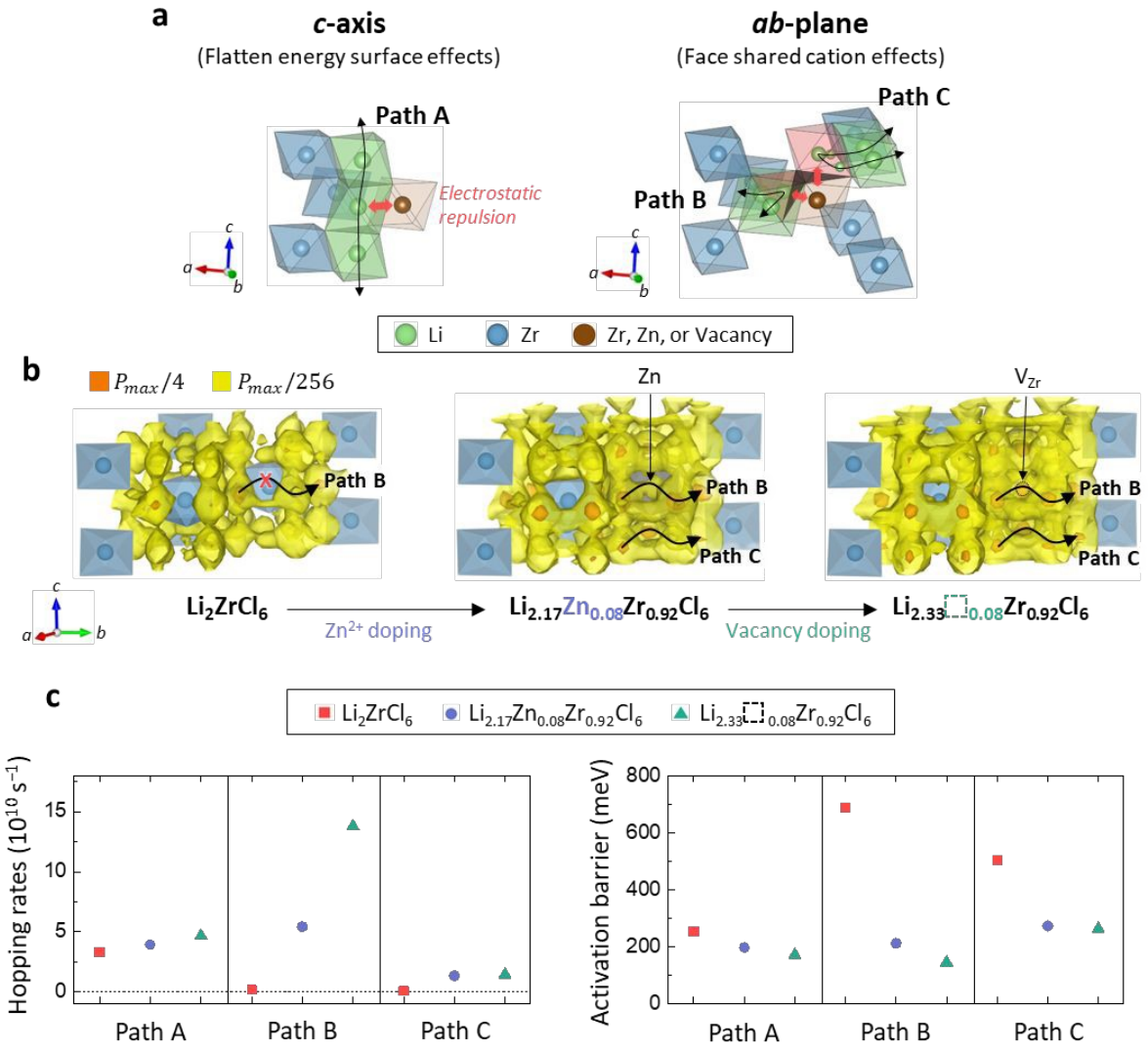

Figure 2. Pathway-resolved analysis of local lithium diffusion kinetics as a function of aliovalent substitution. (a) Schematic of the three primary local diffusion pathways around a substituent site. **Path A** represents *c*-axis diffusion *via* an edge-sharing octahedron. **Paths B** and **C** represent *ab*-plane diffusion through face-sharing tetrahedral and octahedral sites, respectively. **(b)** lithium probability density isosurfaces for each pathway in the pristine, Zn^{2+}-substituted, and vacancy-substituted models. The orange and yellow surfaces represent $\boldsymbol{P = P_{max}/4}$ and $\boldsymbol{P = P_{max}/256}$, respectively (at 500 K). **(c)** Calculated hopping rates (left) and activation barrier (right) for each specific pathway (**Paths A**, **B**, and **C**) in the three different models: pristine Li_2ZrCl_6 (red), $Li_{2.17}Zn_{0.08}Zr_{0.92}Cl_6$ (blue), and $Li_{2.33}Zr_{0.92}Cl_6$ (green).

View Article Online
DOI: 10.1039/D6EB00070C

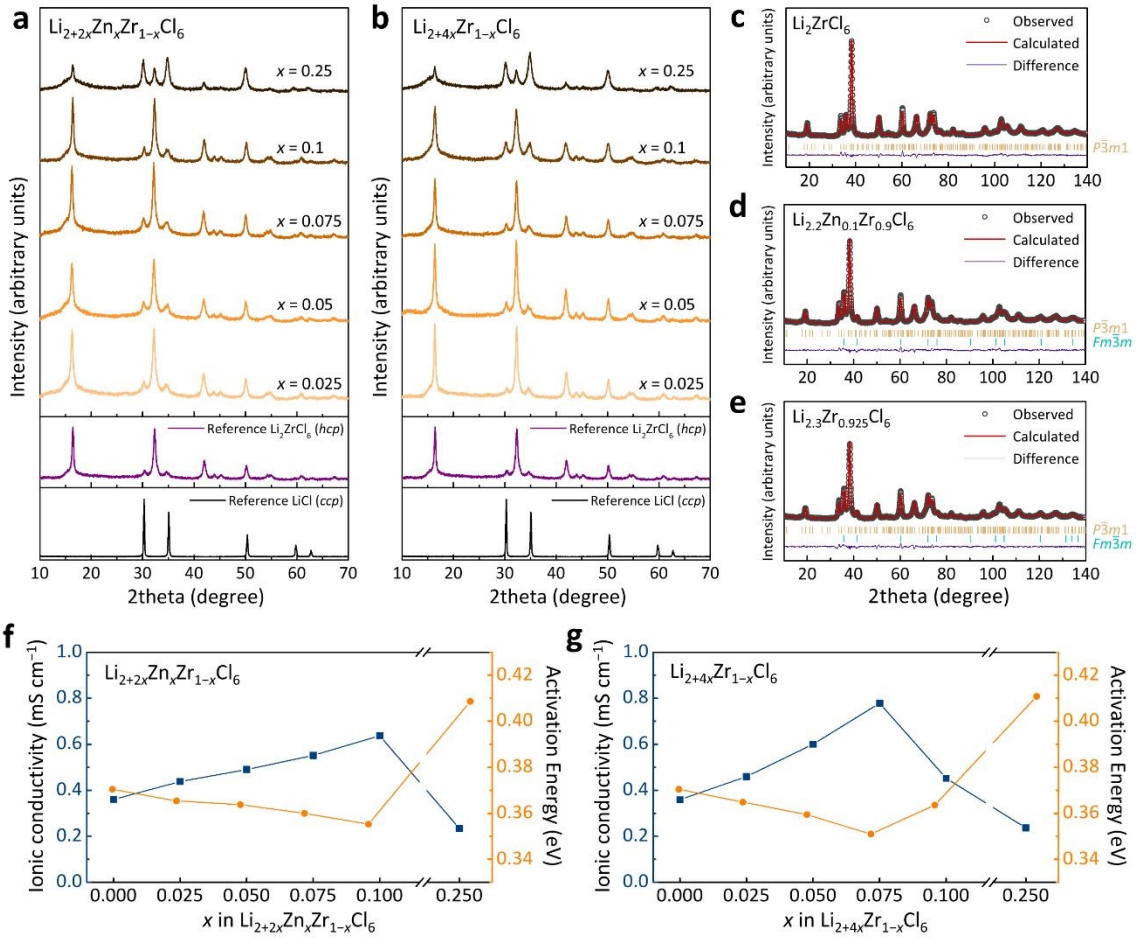

Figure 3. Structural characterization and ionic transport properties of $Li_{2+2x}Zn_xZr_{1-x}Cl_6$ and $Li_{2+4x}Zr_{1-x}Cl_6$ (x = 0–0.25). (a, b) X-ray diffraction patterns for **(a)** the $Li_{2+2x}Zn_xZr_{1-x}Cl_6$ series and **(b)** the $Li_{2+4x}Zr_{1-x}Cl_6$ series (x = 0–0.25). Reference patterns for pristine Li_2ZrCl_6 (*hcp*) and LiCl (*ccp*) are provided for structural comparison. **(c–e)** Rietveld refinement profiles of neutron diffraction data for **(c)** Li_2ZrCl_6, **(d)** $Li_{2.2}Zn_{0.1}Zr_{0.9}Cl_6$, and **(e)** $Li_{2.3}Zr_{0.925}Cl_6$. **(f, g)** Arrhenius plots showing the ionic conductivities (left axis, blue) and corresponding activation energies (right axis, orange) for **(f)** the Zn^{2+}-substituted series and **(g)** the vacancy-substituted series.

View Article Online
DOI: 10.1039/D6EB00070C

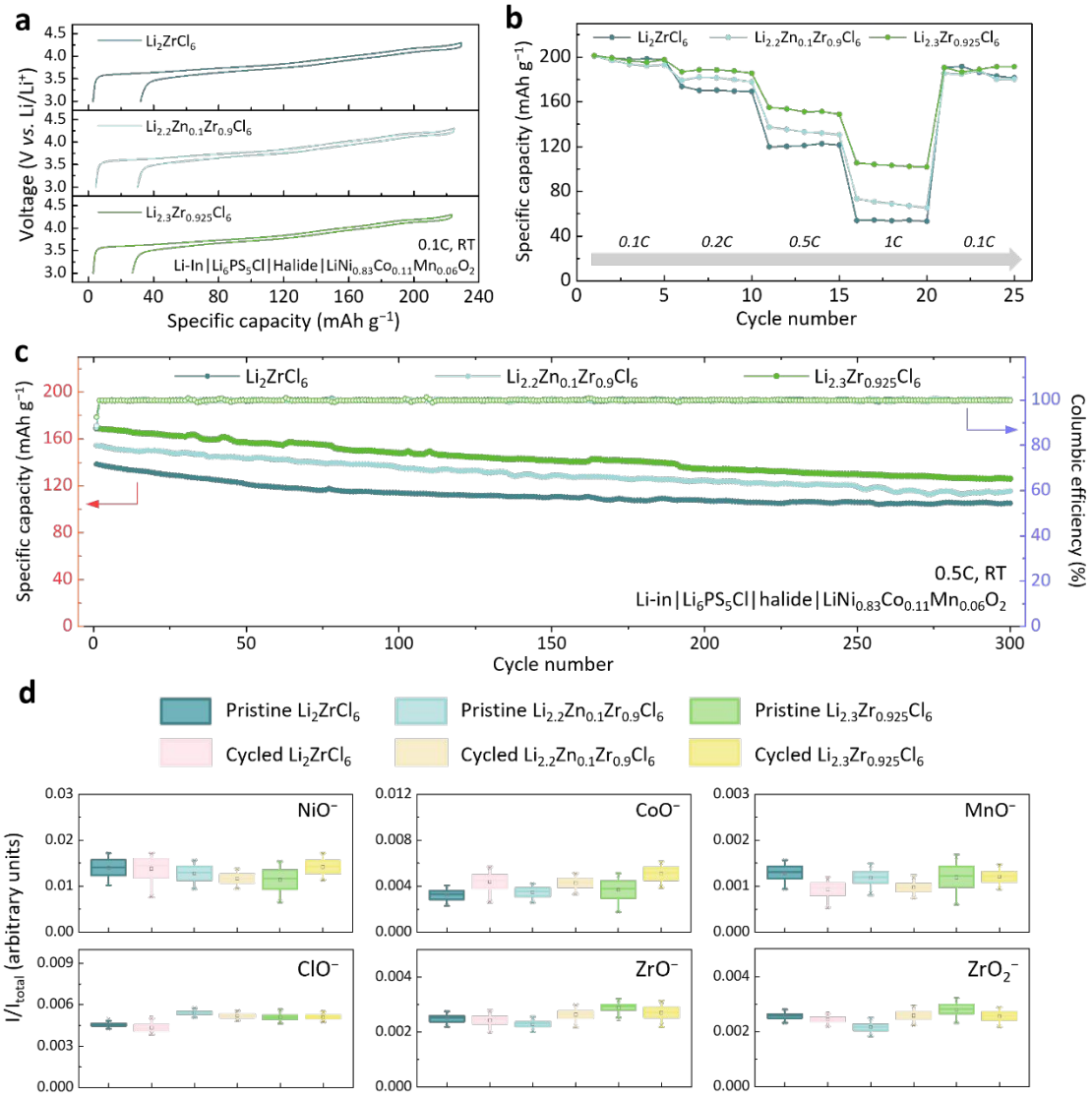

Figure 4. Electrochemical performance and interfacial stability of all-solid-state batteries employing pristine and substituted Li_2ZrCl_6 solid electrolytes. (a) Initial charge/discharge voltage profiles at 0.1C for all-solid-state cells employing pristine Li_2ZrCl_6, Zn-doped $Li_{2.2}Zn_{0.1}Zr_{0.9}Cl_6$, and vacancy-doped $Li_{2.3}Zr_{0.925}Cl_6$ as the solid electrolyte with a single-crystal $LiNi_{0.83}Co_{0.11}Mn_{0.06}O_2$ cathode. **(b)** Rate capability comparison of the corresponding cells at current densities ranging from 0.1C to 1C. **(c)** Cycling performance of the corresponding cells after a formation cycle at a rate of 0.5C over 300 cycles. Filled and open circles represent specific capacity (left axis) and Coulombic efficiency (right axis), respectively. **(d)** Time-of-Flight Secondary Ion Mass Spectrometry results for the composite cathode before and after 300 cycles. The upper panels display signals corresponding to cathode-derived fragments (NiO^-, MnO^- and CoO^-), while the lower panels show electrolyte-derived fragments (ClO^-, ZrO^- and ZrO_2^-).

View Article Online
DOI: 10.1039/D6EB00070C

Author contributions

J.N. and S.Y. contributed equally to this work. Joohyeon Noh: Conceptualization, Data curation, Formal analysis, Investigation, Methodology, Validation, Visualization, Writing – original draft, Writing – review and editing. **Seungju Yu**: Data curation, Formal analysis, Methodology, Validation, Visualization, Writing – original draft, Writing – review and editing. **Sunyoung Lee**: Investigation, Methodology, Validation. **Wonju Kim**: Methodology, Validation. **Kyungho Yoon**: Methodology, Validation. **Sangwook Han**: Methodology. **Junhyuk Song**: Methodology. **Kyungbae Oh**: Methodology, Formal analysis. **Chanwoong Park**: Validation. **Daero Won**: Methodology. **Geunji Choi**: Methodology. **Kangtaek Lee**: Methodology. **Kisuk Kang**: Conceptualization, Investigation, Methodology, Project administration, Validation, Visualization, Supervision, Writing – original draft, Writing – review and editing.

Conflicts of interest

There are no conflicts to declare.

Data availability

The data supporting this article have been included as part of the Supplementary Information.

Acknowledgements

This work was supported by the National Research Foundation of Korea (NRF) grant funded by the Korea government (Ministry of Science and ICT, No. RS-2023-00261543 and RS-2021-NR057375) This work was also supported by the research program of LOTTE Energy Materials.

References

1. Q. Zhao, S. Stalin, C.-Z. Zhao and L. A. Archer, *Nat. Rev. Mater.*, 2020, **5**, 229-252.

View Article Online
DOI: 10.1039/D6EB00070C

2. J. Janek and W. G. Zeier, *Nat. Energy*, 2016, **1**, 16141.
3. C. Wang and X. Sun, *Engineering*, 2023, **21**, 32-35.
4. J. T. Frith, M. J. Lacey and U. Ulissi, *Nat. Commun.*, 2023, **14**, 420.
5. Z. Zhang, Y. Shao, B. Lotsch, Y.-S. Hu, H. Li, J. Janek, L. F. Nazar, C.-W. Nan, J. Maier, M. Armand and L. Chen, *Energy Environ. Sci.*, 2018, **11**, 1945-1976.
6. R. Chen, Q. Li, X. Yu, L. Chen and H. Li, *Chem. Rev.*, 2020, **120**, 6820-6877.
7. J. Janek and W. G. Zeier, *Nat. Energy*, 2023, **8**, 230-240.
8. E. P. Alsaç, D. L. Nelson, S. G. Yoon, K. A. Cavallaro, C. Wang, S. E. Sandoval, U. D. Eze, W. J. Jeong and M. T. McDowell, *Chem. Rev.*, 2025, **125**, 2009-2119.
9. X. Li, J. Liang, X. Yang, K. R. Adair, C. Wang, F. Zhao and X. Sun, *Energy Environ. Sci.*, 2020, **13**, 1429-1461.
10. C. Wang, J. Liang, J. T. Kim and X. Sun, *Sci. Adv.*, 2022, **8**, eadc9516.
11. Y. Ren, T. Danner, A. Moy, M. Finsterbusch, T. Hamann, J. Dippell, T. Fuchs, M. Müller, R. Hoft, A. Weber, L. A. Curtiss, P. Zapol, M. Klenk, A. T. Ngo, P. Barai, B. C. Wood, R. Shi, L. F. Wan, T. W. Heo, M. Engels, J. Nanda, F. H. Richter, A. Latz, V. Srinivasan, J. Janek, J. Sakamoto, E. D. Wachsman and D. Fattakhova-Rohlfing, *Adv. Energy Mater.*, 2022, **13**, 2201939.
12. S.-K. Jung, H. Gwon, S.-S. Lee, H. Kim, J. C. Lee, J. G. Chung, S. Y. Park, Y. Aihara and D. Im, *J. Mater. Chem. A*, 2019, **7**, 22967-22976.
13. K. Yoon, J.-J. Kim, W. M. Seong, M. H. Lee and K. Kang, *Sci. Rep.*, 2018, **8**, 8066.
14. K. Yoon, H. Kim, S. Han, T.-S. Chan, K.-H. Ko, S. Jo, J. Park, S. Kim, S. Lee, J. Noh, W. Kim, J. Lim and K. Kang, *Appl. Phys. Rev.*, 2022, **9**, 031403.
15. Y. Zhai, W. Kang, Y. Li, N. Zhang, X. Liu, R. An, C. Yang, X. Zhu, Q. Huang, L. Chen, D. Cao, M. Wang, Y. Lu, J. Li, Z. Xiong, C. Feng, H. Jin, Y. Guan, Y. Su, F. Wu and N. Li, *Energy Mater. Adv.*, 2025, **6**, 0163.
16. T. Asano, A. Sakai, S. Ouchi, M. Sakaida, A. Miyazaki and S. Hasegawa, *Adv. Mater.*, 2018, **30**, e1803075.
17. X. Li, J. Liang, J. Luo, M. Norouzi Banis, C. Wang, W. Li, S. Deng, C. Yu, F. Zhao, Y. Hu, T.-K. Sham, L. Zhang, S. Zhao, S. Lu, H. Huang, R. Li, K. R. Adair and X. Sun, *Energy Environ. Sci.*, 2019, **12**, 2665-2671.
18. L. Zhou, C. Y. Kwok, A. Shyamsunder, Q. Zhang, X. Wu and L. F. Nazar, *Energy Environ. Sci.*, 2020, **13**, 2056-2063.

View Article Online
DOI: 10.1039/D6EB00070C

19. J. Liang, X. Li, S. Wang, K. R. Adair, W. Li, Y. Zhao, C. Wang, Y. Hu, L. Zhang, S. Zhao, S. Lu, H. Huang, R. Li, Y. Mo and X. Sun, *J. Am. Chem. Soc.*, 2020, **142**, 7012-7022.
20. S. Muy, J. Voss, R. Schlem, R. Koerver, S. J. Sedlmaier, F. Maglia, P. Lamp, W. G. Zeier and Y. Shao-Horn, *iScience*, 2019, **16**, 270-282.
21. S. Y. Kim, K. Kaup, K.-H. Park, A. Assoud, L. Zhou, J. Liu, X. Wu and L. F. Nazar, *ACS Mater. Lett.*, 2021, **3**, 930-938.
22. J. Liang, E. van der Maas, J. Luo, X. Li, N. Chen, K. R. Adair, W. Li, J. Li, Y. Hu, J. Liu, L. Zhang, S. Zhao, S. Lu, J. Wang, H. Huang, W. Zhao, S. Parnell, R. I. Smith, S. Ganapathy, M. Wagemaker and X. Sun, *Adv. Energy Mater.*, 2022, **12**, 2103921.
23. A. Zheng, L. Luo, L. Li, Z. Jiang, S. Ma and J. Yu, *J. Mater. Chem. A*, 2025, **13**, 6067-6074.
24. S. Yu, J. Noh, B. Kim, J.-H. Song, K. Oh, J. Yoo, S. Lee, S.-O. Park, W. Kim, B. Kang, D. Kil and K. Kang, *Science*, 2023, **382**, 573-579.
25. L. Huang, L. Zhang, J. Bi, T. Liu, Y. Zhang, C. Liu, J. Cui, Y. Su, B. Wu and F. Wu, *Energy Mater. Adv.*, 2024, **5**, 0092.
26. Z. Liu, P.-H. Chien, S. Wang, S. Song, M. Lu, S. Chen, S. Xia, J. Liu, Y. Mo and H. Chen, *Nat. Chem.*, 2024, **16**, 1584-1591.
27. H. Kwak, S. Wang, J. Park, Y. Liu, K. T. Kim, Y. Choi, Y. Mo and Y. S. Jung, *ACS Energy Lett.*, 2022, **7**, 1776-1805.
28. K. Wang, Q. Ren, Z. Gu, C. Duan, J. Wang, F. Zhu, Y. Fu, J. Hao, J. Zhu, L. He, C. W. Wang, Y. Lu, J. Ma and C. Ma, *Nat. Commun.*, 2021, **12**, 4410.
29. H. Kwak, D. Han, J. Lyoo, J. Park, S. H. Jung, Y. Han, G. Kwon, H. Kim, S. T. Hong, K. W. Nam and Y. S. Jung, *Adv. Energy Mater.*, 2021, **11**, 2003190.
30. S. Chen, C. Yu, S. Chen, L. Peng, C. Liao, C. Wei, Z. Wu, S. Cheng and J. Xie, *Chin. Chem. Lett.*, 2022, **33**, 4635-4639.
31. Q. Shao, C. Yan, M. Gao, W. Du, J. Chen, Y. Yang, J. Gan, Z. Wu, W. Sun, Y. Jiang, Y. Liu, M. Gao and H. Pan, *ACS Appl. Mater. Interfaces*, 2022, **14**, 8095-8105.
32. S. Chen, C. Yu, C. Wei, Z. Jiang, Z. Zhang, L. Peng, S. Cheng and J. Xie, *Energy Mater. Adv.*, 2023, **4**, 0019.
33. Z. Yao, Q. Jia, J. Xiang, F. Tu, J. Shi, Y. Zhang, J. Huang, Y. Jiang, W. Gong and D. Yang, *J. Electron. Mater.*, 2024, **54**, 1021-1028.

View Article Online
DOI: 10.1039/D6EB00070C

34. K. Kim, D. Park, H. G. Jung, K. Y. Chung, J. H. Shim, B. C. Wood and S. Yu, *Chem. Mater.*, 2021, **33**, 3669-3677.
35. D. Luo, H. Zhu, Y. Xia, Z. Yin, Y. Qin, T. Li, Q. Zhang, L. Gu, Y. Peng, J. Zhang, K. M. Wiaderek, Y. Huang, T. Yang, Y. Tang, S. Lan, Y. Ren, W. Lu, C. M. Wolverton and Q. Liu, *Nat. Energy*, 2023, **8**, 1078-1087.
36. K. S. Kang, Y. S. Meng, J. Breger, C. P. Grey and G. Ceder, *Science*, 2006, **311**, 977-980.
37. A. Van der Ven and G. Ceder, *J. Power Sources*, 2001, **97-98**, 529-531.
38. R. D. Shannon, *Acta Crystallogr. Sect. A*, 1976, **32**, 751-767.
39. N. J. J. de Klerk, E. van der Maas and M. Wagemaker, *ACS Appl. Energy Mater.*, 2018, **1**, 3230-3242.
40. H. Guo, V. Koverga, S. C. Selvaraj and A. T. Ngo, *ACS Appl. Energy Mater.*, 2025, **8**, 14773-14790.
41. Y. C. Lee and S. C. Jung, *Electrochim. Acta*, 2024, **497**, 144632.
42. G. Yang, X. Liang, S. Zheng, H. Chen, W. Zhang, S. Li and F. Pan, *eScience*, 2022, **2**, 79-86.
43. X. He, Y. Zhu and Y. Mo, *Nat. Commun.*, 2017, **8**, 15893.
44. Y. Xiao, K. Jun, Y. Wang, L. J. Miara, Q. Tu and G. Ceder, *Adv. Energy Mater.*, 2021, **11**, 2101437.
45. J. Liang, X. Li, S. Wang, K. R. Adair, W. Li, Y. Zhao, C. Wang, Y. Hu, L. Zhang, S. Zhao, S. Lu, H. Huang, R. Li, Y. Mo and X. Sun, *J. Am. Chem. Soc.*, 2020, **142**, 7012-7022.
46. X. Li, J. Liang, J. Luo, M. Norouzi Banis, C. Wang, W. Li, S. Deng, C. Yu, F. Zhao, Y. Hu, T.-K. Sham, L. Zhang, S. Zhao, S. Lu, H. Huang, R. Li, K. R. Adair and X. Sun, *Energy Environ. Sci.*, 2019, **12**, 2665-2671.
47. Q. Wang, Y. Zhou, X. Wang, H. Guo, S. Gong, Z. Yao, F. Wu, J. Wang, S. Ganapathy, X. Bai, B. Li, C. Zhao, J. Janek and M. Wagemaker, *Nat. Commun.*, 2024, **15**, 1050.
48. J. Noh, M. Kim, S. Yu, W. Kim, J. Yoo, S. Lee, S. Han, D. Won, C. Park, G. Choi and K. Kang, *Solid State Ionics*, 2025, **428**.
49. H.-J. Jeon, Y. Subramanian and K.-S. Ryu, *J. Power Sources*, 2024, **602**, 234343.
50. X. Liu, F. Mi and C. Sun, *Chem. Commun.*, 2025, **61**, 1144-1147.
51. H. Zhang, Z. Yu, H. Chen, Y. Zhou, X. Huang and B. Tian, *J. Energy Chem.*, 2023, **79**, 348-356.

View Article Online
DOI: 10.1039/D6EB00070C

52. I. Kochetkov, T.-T. Zuo, R. Ruess, B. Singh, L. Zhou, K. Kaup, J. Janek and L. Nazar, *Energy Environ. Sci.*, 2022, **15**, 3933-3944.

View Article Online
DOI: 10.1039/D6EB00070C

Data Availability Statement

The data supporting this article have been included as part of the Supplementary Information.